Check for updates

Spin photonic forces in non-reciprocal waveguides

SARANG PENDHARKER,[1,2] FARID KALHOR,[3] TODD VAN MECHELEN,[3] SAMAN JAHANI,[3] NEDA NAZEMIFARD,[4] THOMAS THUNDAT,[4] AND ZUBIN JACOB[2,3,*]

[1]*Department of Electronics and Electrical Communication Engineering, Indian Institute of Technology Kharagpur, W. Bengal 721302, India*
[2]*Department of Electrical and Computer Engineering, University of Alberta, Edmonton, Alberta T6G 1H9, Canada*
[3]*Birck Nanotechnology Center and Purdue Quantum Center, School of Electrical and Computer Engineering, Purdue University, West Lafayette, IN 47906, USA*
[4]*Department of Chemical and Materials Engineering, University of Alberta, Edmonton, Alberta T6G 1H9, Canada*
[*]*zjacob@purdue.edu*

Abstract: Optical forces acting on particles - controlled by the intensity, polarization and direction of optical beams - have become an important tool in manipulation, sorting and analysis of nano/micro-particles. The nature of these forces has been well understood in reciprocal structures exhibiting time-reversal symmetries. Here, we investigate the nature of optical forces in non-reciprocal structures with non-degenerate counter-propagating modes. We consider the specific case of non-reciprocity induced via translational motion and show that the two counter-propagating modes in a moving slab-waveguide are not degenerate which results in a non-zero lateral and longitudinal force on a nanoparticle. We prove that these anomalous forces are fundamentally connected to near-field photonic spin in optical waveguides and explain their directionality using universal spin-momentum locking of evanescent waves. The presented results show that the interplay of photon spin and non-reciprocity can lead to unique avenues of controlling nanoscale optical forces on-chip.

1. Introduction

The use of controlled optical forces has evolved into an important tool for analysis, manipulation and sorting of nanoparticles [1–5]. These optical forces depend on the intensity, direction and polarization of the optical beam, which can be manipulated to precisely control the nanoparticles. Among the optical forces, an anomalous lateral force acting on chiral particles is of particular interest, as it strongly depends on the chirality of the particle and acts in a direction transverse to the radiation pressure and the gradient force [6–14]. The lateral force can therefore be efficiently employed to optically separate molecules and particles based on their chirality, which is otherwise a challenging task in chemistry and biology [3]. The magnitude and direction of this anomalous lateral force depends on the transverse spin-density of the optical beam and is reported to be locked to the momentum of the optical beam [15]. The origin of this momentum-locked lateral optical force is in the, recently reported, universal spin-momentum locking in electromagnetic waves [16, 17]. Locking of the optical spin with the direction of propagation (momentum) is similar to the phenomena known for electronic surface states [18, 19], and also explains the polarization-dependent directional propagation of optical modes and surface plasmon polaritons reported in recent experiments [20–23]. This phenomenon also occurs for spontaneous emission and scattering from 2D materials due to circularly polarized light emission [24].

The origin of spin-momentum locking was found by Mechelen. et. al [16] to be inherent to

the nature of evanescent optical waves, which forms a right-handed triplet of spin, momentum and direction of attenuation in any evanescent wave.

$$\hat{s} = \hat{k} \times \hat{\eta}, \tag{1}$$

here $\hat{k}$ is the direction of propagation (momentum), $\hat{\eta}$ is the direction of decay of the evanescent field and $\hat{s}$ is the direction of transverse spin. This spin-momentum locking is universal and can be observed in various waveguiding structures such as slab-waveguides, surface plasmons, and optical fibers [15, 25–30]. The specific case of optical forces at total internal reflection was studied [15] and also experimentally demonstrated recently [8]. At optical frequencies this effect is tied to causal boundary conditions on evanescent waves which transfer this spin-momentum locking to bulk guided modes. At microwave frequencies, where perfect metallic boundary conditions are allowed, the longitudinal component of the electric field gives rise to similar spin-momentum locking effects in waveguides. Note, we do not address this effect by "chiral" optics so as to avoid confusion with chiral nanoparticles where magnetic response is fundamentally necessary. The difference between chiral dipole emission and spin-polarized dipole emission is that a chiral dipole emits directionally even when placed at the center of the waveguide. A detailed analysis of this effect can be found in [16]. We emphasize that spin-momentum locking in waveguides, plasmons, optical fibers is a classical phenomenon and not related to any quantum or topological phenomenon.

Figure 1 displays the architecture for on-chip spin photonics. It shows the schematic of a ridge waveguide and the observed universal spin-momentum locking with the locked triplet of spin, momentum and decay. The waveguide has a fundamental TE-like mode. This mode has dominant electric spin-density in the $\hat{z}$ direction and dominant magnetic spin-density in the $\hat{y}$ direction. The direction of the spin-density is governed by the spin-momentum locking right-hand rule [Eq. (1)]. In a reciprocal optical structure, the positive- and negative-momentum modes are degenerate and therefore the spin-density (and hence the optical force) switches its sign, while conserving the magnitude, with reversal of the momentum. However, the non-reciprocity in wave propagation can break the degeneracy of positive- and negative-momentum modes and open up a new dimension in the control of optical forces on nanoparticles. We emphasize that the direction of the spin photonic force on a chiral particle is governed by the right handed triplet rule.

In this paper, we explore the interplay of spin photonics and non-reciprocity in waveguides. We consider the special case of non-reciprocity induced by motion of a slab waveguide, a situation which physically occurs when there is a relative motion between a particle and an optical structure. We show that the degeneracy of positive- and negative-momentum modes in a non-reciprocal (moving) waveguide is broken, and results in an unbalanced transverse and longitudinal optical force. Here we present the transformation of waveguide modes as observed by a particle moving near a slab waveguide, and show the non-degeneracy of the positive- and negative-momentum waves. We further show that the transverse polarization (spin) switches from RHC to LHC while remaining locked to the momentum, as the velocity of propagation approaches the Cherenkov velocity. Finally, we compute the optical recoil force and radiation pressure force on a chiral particle interacting with the evanescent fields of two counter-propagating modes in a moving slab-waveguide. Our simulations show the existence of unbalanced forces that are proportional to the magnitude of the velocity and form an important step in understanding the nature of spin-photonic forces on moving-particles. Although we have analyzed the case of non-reciprocity induced by moving media, a similar phenomenon can be expected in non-reciprocal optical devices realized by magnetoplasmonic structures [31, 32], or by recently reported opto-mechanically induced non-reciprocity [33, 34]. Such motion induced non-reciprocity is widely used in Fiber Optic Gyroscopes (FOG) [35] and is still an active area of research [36–38]. Recently, Weernink et al. have studied forces induced by breaking time-reversal symmetry in a rotating particle near a planar surface [39] and similar systems can
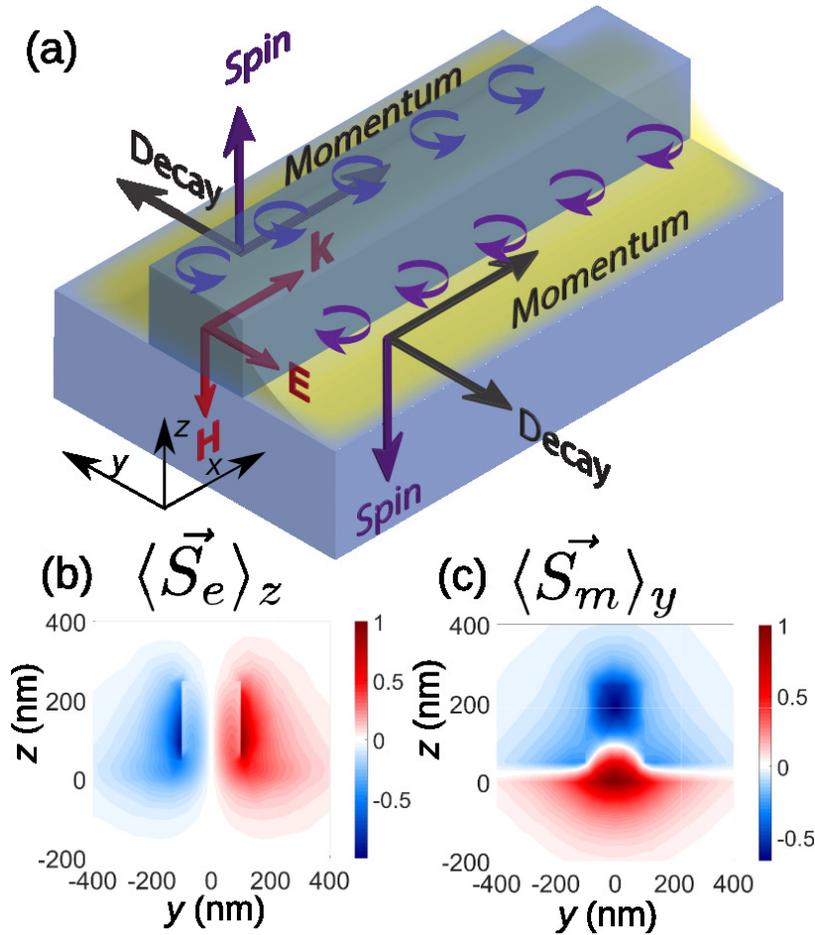
Fig. 1. Spin-momentum locking in a ridge waveguide. (a) Schematic of a ridge waveguide and the EM triplet introduced by Mechelen et. al. [16], for the fundamental TE-like mode. (b) $\hat{z}$ component of electric spin-density $\langle \vec{S_e} \rangle$ in y-z plane for the fundamental mode. (c) $\hat{y}$ component of magnetic spin-density $\langle \vec{S_m} \rangle$ in y-z plane for the fundamental mode.

be used to verify our theoretical predictions.

2. Non-reciprocity in moving waveguides and photon spin

For the analysis of non-reciprocity in moving waveguide structure, we consider a simple slab-waveguide, as it is easier to solve the dispersion curves and compute the modal field profiles for a moving slab-waveguide. We would like to emphasize that the presented phenomena is equally valid in a practical structure, such as ridge waveguide. Let us consider a particle moving with velocity v_{motion} parallel to the interface of a slab-waveguide, such that it interacts with the evanescent fields of the propagating modes, as shown in Fig. 2(a). If the particle is moving in the negative $\hat{x}$ direction, its interaction with the slab-waveguide can be equivalently analyzed as the interaction between a stationary particle and a slab-waveguide moving in $+\hat{x}$ direction. In the proper frame of the particle, the slab waveguide will move with a velocity v_{motion} in the positive $\hat{x}$ direction. As per the Lorentzian transformation of the constitutive properties, the isotropic dielectric of the slab will appear as bianisotropic in the moving frame of the particle [40]. For simplicity, we consider a two dimensional waveguide in the $x - z$ plane with modal propagation
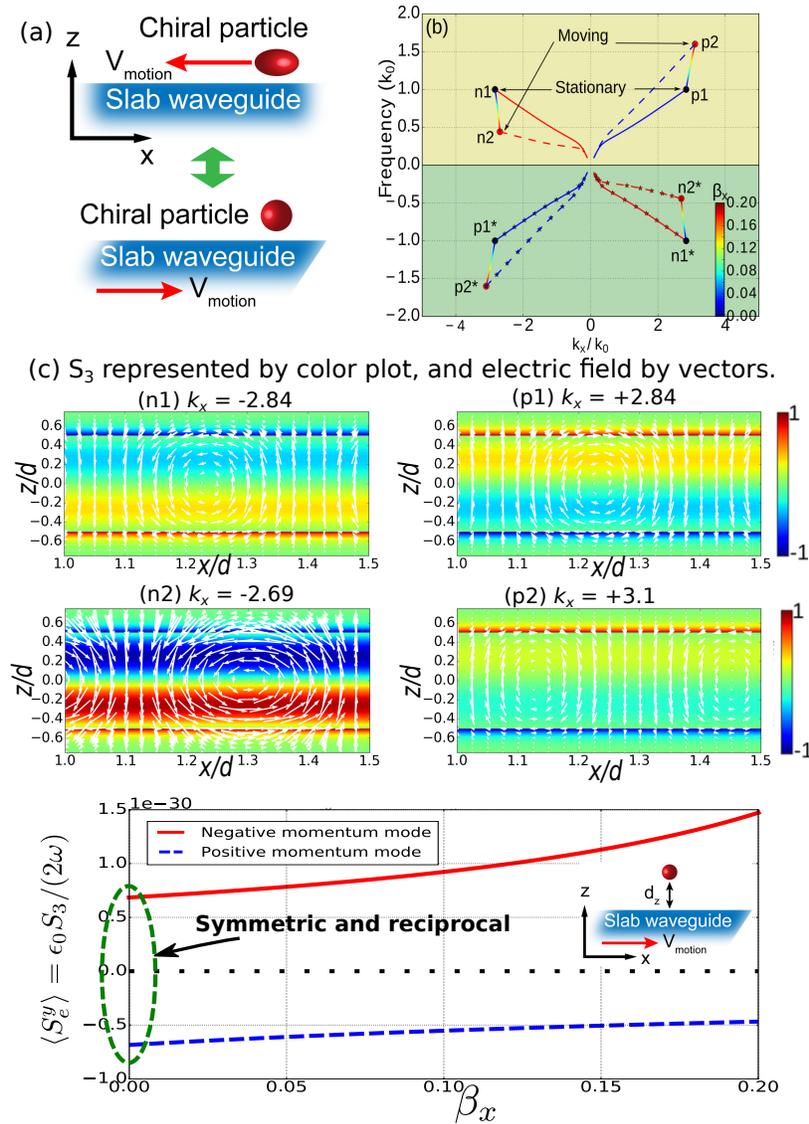
Fig. 2. (a) Schematic of a chiral particle moving near a slab-waveguide. It can be equivalently analyzed by transforming to the frame of the particle where the waveguide is moving instead. (b) The dispersion curves of positive (blue) and negative (red) momentum modes in the full $\omega - k$ plane when the slab is stationary (solid line) and moving (dashed line). The thickness of the waveguide is $d = 1.5 \mu m$ and the dielectric constant is $\epsilon_r = 9$. The frequency axis is normalized to $k_0 = \omega_0/c$, where $\omega_0 = 2\pi 10^{14}$ rad/s. (c) Shows the field plots in the slab-waveguide at points $n1$, $p1$, $n2$ and $p2$. The color plot represents the $\hat{y}$ component of the third Stokes parameter $\vec{S_3} = S_3 \hat{y}$ and the electric field is shown by arrows. (d) The electric-spin density $\langle \vec{S_e} \rangle = \epsilon_0 \vec{S_3}/(2\omega)$ of the positive- and negative-momentum modes as a function of slab velocity at $d_z = 0.1d$, where d is the thickness of the slab.

along $\hat{x}$ direction. Our calculations are fully relativistic and the details can be found in the appendix [41].

Figure 2(b) shows the TM-mode dispersion curves of the stationary and moving slab waveguide

in the full $\omega - k$ plane. The frequency is normalized with velocity of light such that $k_0 = \omega/c$. The solid curves represent the stationary case, while the dashed curves represent the dispersion curves when the slab is moving with normalized velocity $\beta_x = v_{motion}/c = 0.2$. The stationary slab-waveguide is a reciprocal structure with symmetric as well as degenerate positive-momentum ($k_x > 0$) and negative-momentum ($k_x < 0$) modes. However, the moving slab-waveguide is a non-reciprocal structure because of the bianisotropy and asymmetric Doppler transformation of the positive-momentum and negative-momentum modes. A positive mode $p1$ undergoes a blue-shift (increase in the frequency) to a point $p2$, while a negative-momentum mode $n1$ undergoes red-shift (decrease in the frequency) to a point $n2$. The transformation of the points $n1$ and $p1$ as a function of normalized velocity of motion (β_x) is shown by the colored line, where the color mapping of β_x is quantified by the inset colorbar in Fig. 2(b). The negative-frequency region of the plane represents the complex conjugate component of the propagating wave solution. It can be seen that for a moving slab-waveguide, the propagation characteristics are asymmetrical and non-reciprocal.

Figure 2(c) displays the field plots at the four specific points ($n1$, $p1$, $n2$, $p2$) in the $\omega - k$ plane. To quantify the non-degeneracy of positive and negative propagating modes, we compute the electric spin-density $\langle \vec{S_e} \rangle$ in the evanescent wave region. Here we analyze both the third Stokes parameter $\vec{S_3} = \Im(\vec{E}^* \times \vec{E})$, which quantifies the local direction and magnitude of circular polarization, and the associated spin-density $\langle \vec{S_e} \rangle = \epsilon_0 \vec{S_3}/(2\omega)$ of electromagnetic waves. The spin-density represents a dynamical quantity and provides a measure of the local spin angular momentum (SAM) contained in the field. This is closely related but not equivalent to the third Stokes parameter. The electric field profile is represented by the vector plot (arrows), while the circular electric polarization $\vec{S_3}$ normalized between $(-1, 1)$ is shown by the color plot. In the stationary case, the electric field profile is symmetrical for both positive- ($p1$) and negative-momentum ($n1$) modes, with the sign of $\vec{S_3}$ flipped with the momentum (k_x) throughout. However, for a moving-slab waveguide, the field strength and spin-density differs for the corresponding $p2$ and $n2$ modes -because of the bianisotropy- resulting in non-degeneracy of positive- and negative-momentum modes. Note, the magnetic spin-density vanishes for TM modes. Figure 2(d) shows $\langle \vec{S_e} \rangle$ as a function of slab velocity (β_x) at a distance $d_z = 0.1d$ from the interface of the waveguide. When the slab is stationary, $\beta_x = 0$, the spin-densities of the positive-momentum and negative-momentum modes are equal and opposite. Conversely, when the slab starts moving, the breaking of degeneracy in the positive and negative-momentum leads to asymmetry in $\langle \vec{S_e} \rangle$ for the non-reciprocal slab-waveguide.

For completeness, we also analyze the relativistic case when the velocity of motion is greater then the Cherenkov threshold velocity. Figure 3(a) shows the transformation of positive- and negative-momentum modes for this relativistic regime. It is physically possible for a fast moving relativistic particle to observe the waveguide as moving with velocity greater than the Cherenkov velocity ($v_{motion} > \omega/k_x$) since the phase velocity in a stationary waveguide is less then the velocity of light. When the velocity is large enough ($v_{motion} > \omega/k_x$), the complex-conjugate component of the negative-momentum mode is transformed to the positive-momentum positive-frequency region, resulting in flipping of negative-momentum to positive-momentum. A similar transformation for plasmonic mode in moving metal-insulator-metal waveguide structure is explained in detail in [41]. This essentially means that the slab-waveguide is moving fast enough for the backward propagating mode to appear as forward propagating in the reference frame of the particle; consequently switching the sign of momentum from negative to positive at the Cherenkov velocity. Since the polarization state of the evanescent wave is locked to the direction of momentum, the near-field polarization also switches from RHC to LHC, as shown in the Fig. 3(b). As the mode transformation approaches Cherenkov velocity, its frequency approaches the zero limit $k_0 \rightarrow 0$. This is a quasi-static limit, where the phase-front appears stationary and the magnetic field vanishes. At this point, the spin-density diverges $\langle \vec{S_e} \rangle \rightarrow \infty$. However, this
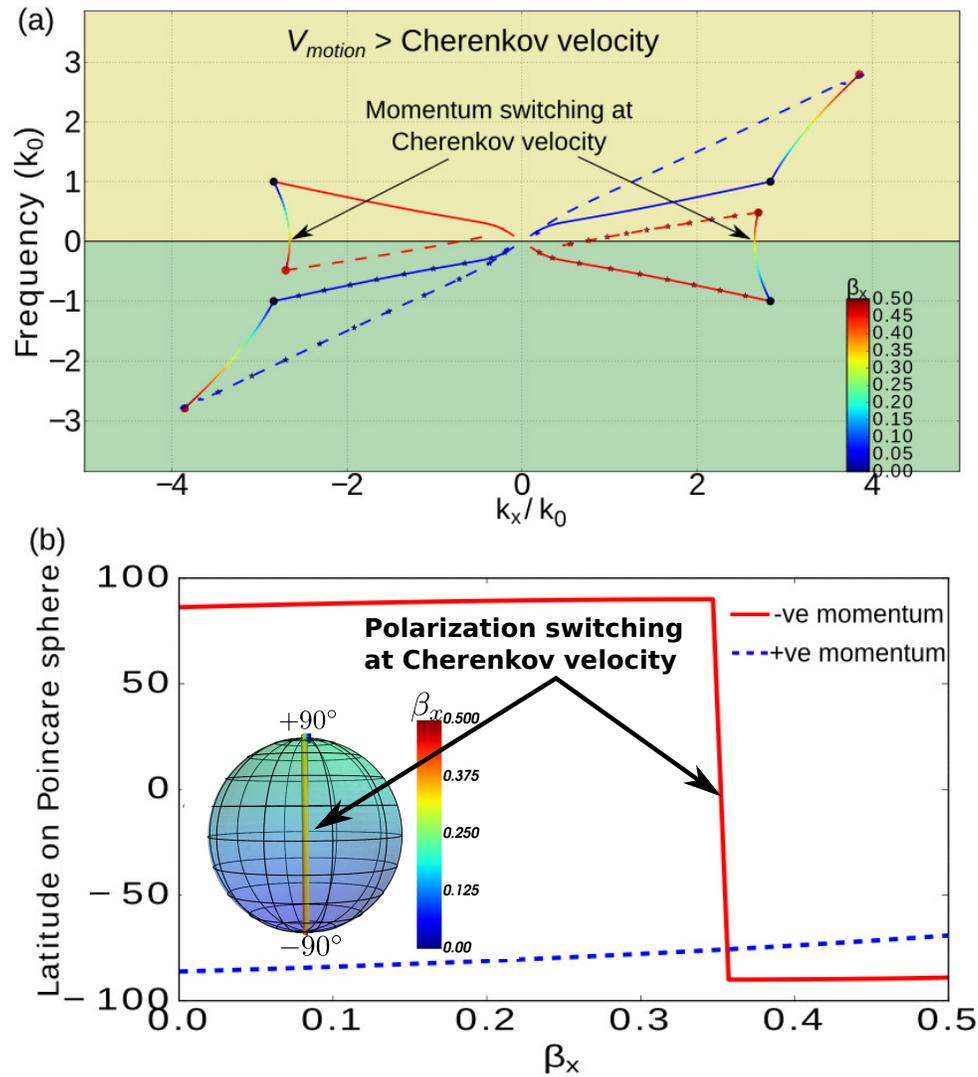
Fig. 3. Velocity of motion greater than Cherenkov velocity. (a) Dispersion curves in the moving slab waveguide when the velocity of motion is large enough to transform the negative frequency modes to the positive frequency region. Above the Cherenkov velocity the negative-momentum mode is also transformed to the positive-momentum. (b) Shows the spin of the modes as latitude on the Poincare sphere. It can be seen that the spin switches abruptly from LHC to RHC at the Cherenkov velocity.

does not imply a singularity in polarization $\vec{S}_3$.

The above discussion shows that the spin-density of two counter-propagating modes in a moving waveguide is not balanced. This imbalance can be viewed as motion-induced net spin-density. Note that this spin is zero in a stationary waveguide with degenerate counter-propagating modes. This unbalanced spin results in unbalanced optical forces on a particle interacting with the spin of a moving waveguide.
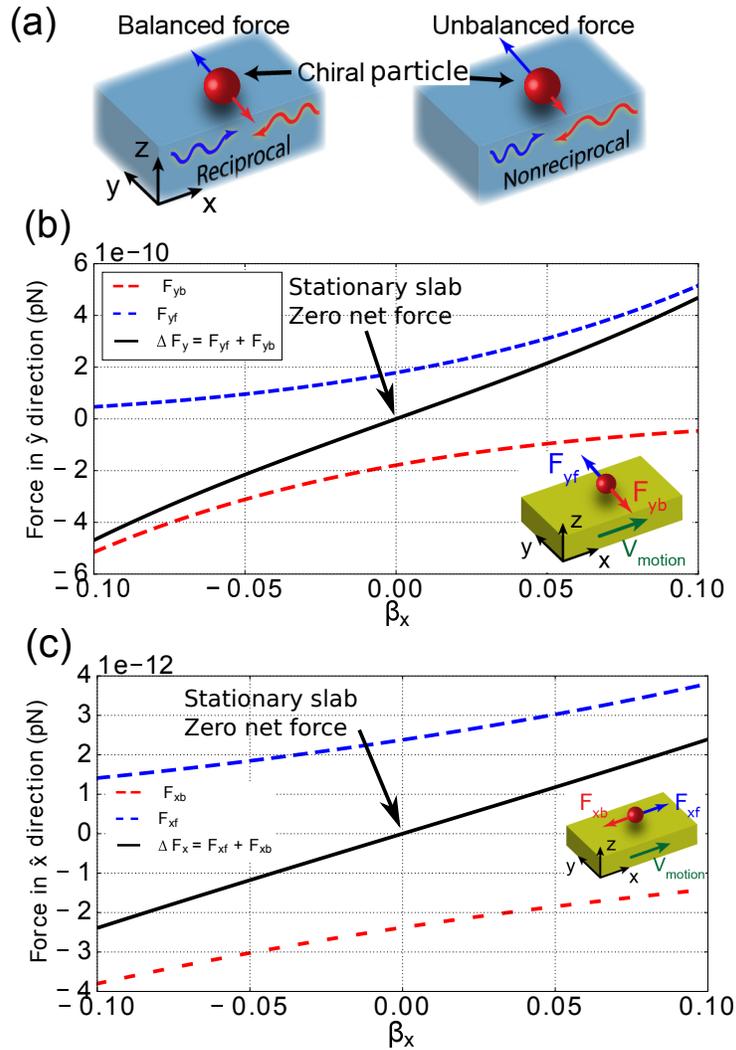
Fig. 4. (a) Two degenerate and counter-propagating modes in a stationary waveguide are symmetric, resulting in a balance of radiation pressure force and scatttering recoil force on a particle in its vicinity. However, when the slab is moving, the two modes transform asymmetrically resulting in an unbalanced force. (b) ΔF_y represents the net optical force on a chiral particle due to the two modes in the lateral direction $\hat{y}$ as function of velocity of motion. F_{yf} and F_{yb} is the force on the particle in $\hat{y}$ direction due to the positive (forward) momentum mode and the negative (backward) momentum mode, respectively.(c) ΔF_x represents the net force in the $\hat{x}$ direction as function of velocity of motion. F_{xf} and F_{xb} represent the force in the $\hat{x}$ direction due to the positive-momentum mode and the negative-momentum mode, respectively. All forces are computed at a distance $0.1d$ from the interface, where $d = 1.5\mu m$ is the thickness of the slab waveguide. For computation of optical force, electric field of the form $E_x = 1e^{i(k_x x - \omega t)}e^{ik_{z2}z}$V/m, is assumed in the region $z > d/2$. This corresponds to the approximate Poynting vector of 17 $\mu W/m^2$ at the center of the stationary waveguide.

3. Longitudinal and transverse photonic forces

First we analyze the stationary waveguide [Fig. 4(a)]. Here, both positive- and negative-momentum modes are simultaneously propagating with identical but reversed properties. Their transverse spin (along $\hat{y}$) at a point near the waveguide interface is equal and opposite for $\beta_x = 0$, as shown in Fig. 2(d). Therefore, the net transverse optical scattering-recoil force resulting from the interaction of electric spin-density and a chiral particle also balances to zero. However, when the particle is moving, it interacts with a moving slab-waveguide in which the positive- and negative-momentum modes are not degenerate, possessing unequal frequency and spin-densities. This results in an unbalanced force whose direction and magnitude depends on the relative velocity between the particle and the slab. The scattering recoil force of a TM-polarized wave is shown in Fig. 4(b) and is primarily along the transverse $\hat{y}$ direction. The blue and red curves represent the force due to the positive- and negative-momentum modes respectively and the net resultant force is represented by the black dashed curve. It can be seen that the resultant force is proportional to the velocity of motion β_x and its sign is reversed with the direction of motion. Here we have assumed a constant polarizability matrix of $\begin{bmatrix} \alpha_{ee} & i\alpha_{em} \\ -i\alpha_{me} & \alpha_{mm} \end{bmatrix} = \begin{bmatrix} 1.2 + i0.01Cm^2/V & i0.01Cm^2/A \\ -i0.01Am^3/V & 0.0002m^3 \end{bmatrix} \times 10^{-24}$ for the chiral particle [15].

Figure 4(c) shows the radiation pressure force acting along the $\hat{x}$ direction. As expected, the radiation pressure force due to individual modes is along the direction of propagation respectively, which results in zero net force for a stationary waveguide (see black dashed curve at $\beta_x = 0$). However, when there is a relative motion between the particle and the sforb-waveguide, the radiation pressure force due to the two counter-propagating modes are unequal, resulting in a net force proportional to the relative velocity. Note that the radiation pressure force exists even for an achiral particle, and the direction of the force is such that it opposes the relative motion between the particle and the waveguide. This is similar to the vacuum drag experienced by a particle moving in the vicinity of a medium and interacting with the thermal fluctuation induced near-fields.

We emphasize that the optical force due to non-reciprocity is a novel observation, which is very different in characteristics from an optical force created by unequal relative strength of two counter-propagating modes.

4. Conclusion

We have shown that non-reciprocity - induced by relative motion- results in (i) longitudinal optical forces in a polarizable particle (ii) lateral force in a chiral particle. The fundamental origin of the lateral force is the spin-momentum locking in the near field. Both these forces are proportional to the velocity, which may lead to velocity sorting of particles. The presented phenomena will be applicable to other structures with dynamically induced non-reciprocities [31, 33] as well as quantum gyro-electric phases of matter [42], and will lead to novel mechanisms to control the trajectories and localization of particles. Exploiting non-reciprocity and transverse photon spin gives an additional degree of freedom in optical force manipulation. A possible experiment to employ the proposed phenomena for segregation of nano-particles based on chirality and velocity will involve integration of optical waveguide with a microfluidic channels. It is also possible to use the phenomenon of total internal reflection to verify the proposed spin photonic force.

Appendix A. TM-modes in a moving-slab waveguide

A.1. Electric and magnetic fields in moving medium

The electric and magnetic fields in a moving-medium are coupled as per Lorentz transformations, resulting in a bianisotropic medium [40]. The electric displacement field $\vec{D}$ and magnetic field intensity $\vec{H}$ are related to the electric field $\vec{E}$ and magnetic flux density $\vec{B}$ as per the following

equation,

$$\begin{bmatrix} c\vec{D} \\ \vec{H} \end{bmatrix} = \begin{bmatrix} c\epsilon_0 \overleftrightarrow{\epsilon} & \overleftrightarrow{\chi} \\ \overleftrightarrow{\eta} & \frac{\overleftrightarrow{\mu}^{-1}}{c\mu_0} \end{bmatrix} \begin{bmatrix} \vec{E} \\ c\vec{B} \end{bmatrix} \tag{2}$$

Here c is the speed of light in vacuum. When the medium is moving along $\hat{x}$ direction with a velocity v_{motion}, such that $\beta_x = v_{motion}/c$, then the matrices $\overleftrightarrow{\epsilon}$, $\overleftrightarrow{\chi}$, $\overleftrightarrow{\eta}$ and $\overleftrightarrow{\mu}^{-1}$ can be written as,

$$\overleftrightarrow{\epsilon} = \gamma^2 \begin{bmatrix} \frac{\epsilon_r}{\gamma^2} & 0 & 0 \\ 0 & \epsilon_r - \beta_x^2 & 0 \\ 0 & 0 & \epsilon_r - \beta_x^2 \end{bmatrix} \tag{3}$$

$$\overleftrightarrow{\chi} = \gamma^2 \sqrt{\frac{\epsilon_0}{\mu_0}} \begin{bmatrix} 0 & 0 & 0 \\ 0 & 0 & -\beta_x(\epsilon_r - 1) \\ 0 & \beta_x(\epsilon_r - 1) & 0 \end{bmatrix} \tag{4}$$

$$\overleftrightarrow{\eta} = \gamma^2 \sqrt{\frac{\epsilon_0}{\mu_0}} \begin{bmatrix} 0 & 0 & 0 \\ 0 & 0 & -\beta_x(\epsilon_r - 1) \\ 0 & \beta_x(\epsilon_r - 1) & 0 \end{bmatrix} \tag{5}$$

$$\overleftrightarrow{\mu}^{-1} = \gamma^2 \begin{bmatrix} \frac{1}{\gamma^2} & 0 & 0 \\ 0 & -\beta_x^2 \epsilon_r + 1 & 0 \\ 0 & 0 & -\beta_x^2 \epsilon_r + 1 \end{bmatrix} \tag{6}$$

where ϵ_r is the relative dielectric constant of the medium in stationary state, and $\gamma = \frac{1}{\sqrt{1-\beta^2}}$. For harmonic fields propagating with wave vector $\vec{k} = k_x\hat{x} + k_y\hat{y} + k_z\hat{z}$, the Maxwell's curl equations can be written as,

$$\overleftrightarrow{k} \cdot \vec{E} = \omega\vec{B} \tag{7}$$

$$\overleftrightarrow{k} \cdot \vec{H} = -\omega\vec{D} \tag{8}$$

where

$$\overleftrightarrow{k} = \begin{bmatrix} 0 & -k_z & k_y \\ k_z & 0 & -k_x \\ -k_y & k_x & 0 \end{bmatrix} \tag{9}$$

For an inplane wave propagation in $x - z$ plane, the $k_y = 0$. From Eqs. (2) and (7-8), we get,

$$\vec{H} = \left[\overleftrightarrow{\eta} + \frac{\overleftrightarrow{\mu}^{-1}}{\mu_0\omega} \cdot \overleftrightarrow{k} \right] \cdot \vec{E} \tag{10}$$

$$\vec{E} = -\left[\omega\epsilon_0 \overleftrightarrow{\epsilon} + \overleftrightarrow{\chi} \cdot \overleftrightarrow{k} \right]^{-1} \cdot \overleftrightarrow{k} \cdot \vec{H} \tag{11}$$

From the above equations, it can also be derived that

$$\left(\frac{\overleftrightarrow{k} \cdot \overleftrightarrow{\mu}^{-1} \cdot \overleftrightarrow{k}}{\omega \mu_0} + \omega \epsilon_0 \overleftrightarrow{\epsilon} + \overleftrightarrow{k} \cdot \overleftrightarrow{\eta} + \overleftrightarrow{\chi} \cdot \overleftrightarrow{k} \right) \cdot \vec{E} = 0 \tag{12}$$

The condition for non-trivial solution of $\vec{E}$ in the above equation gives the general dispersion relation in a moving medium.

$$\det \left(\frac{\overleftrightarrow{k} \cdot \overleftrightarrow{\mu}^{-1} \cdot \overleftrightarrow{k}}{\omega \mu_0} + \omega \epsilon_0 \overleftrightarrow{\epsilon} + \overleftrightarrow{k} \cdot \overleftrightarrow{\eta} + \overleftrightarrow{\chi} \cdot \overleftrightarrow{k} \right) = 0 \tag{13}$$

A.2. Modes in moving-slab waveguide

We assume a 2D slab waveguide in the $x - z$ plane, with modal propagation along $\hat{x}$ direction. The relative dielectric constant of the slab is assumed to be $\epsilon_r = 9$ with thickness $d = 1.5\mu m$, such that it extends from $z = -d/2$ to $z = +d/2$ in the $\hat{z}$ direction. The frequency of the fundamental mode for such a waveguide comes in the range of 100 THz. The expressions for magnetic and electric fields for TM mode in the three regions (i) $-d/2 < z < d/2$ (ii) $z > d/2$ (iii) $z < -d/2$, are

(i) $\underline{-d/2 < z < d/2}$

$$H_y = Ce^{i(k_x x - \omega t)} e^{-ik_{z1} z} + De^{i(k_x x - \omega t)} e^{ik_{z1} z} \tag{14}$$

Electric field in moving-slab waveguide is derived from Eq. (11), by substituting $k_y = 0$ for inplane propagation. The relation between k_x, k_z and ω in given by the dispersion relation of eq(13).

(ii) $\underline{z > d/2}$

$$H_y = Ae^{i(k_x x - \omega t)} e^{ik_{z2} z} \tag{15}$$

(iii) $\underline{z < -d/2}$

$$H_y = Be^{i(k_x x - \omega t)} e^{-ik_{z3} z} \tag{16}$$

In region (ii) and (iii), regular relation between electric and magnetic fields is used to compute the electric fields. Since the direction of motion is perpendicular to the direction of interface between slab and the surrounding vacuum, the boundary conditions on the tangential components of the fields hold true for moving medium as well [40,41]. Boundary conditions are applied at the two interface on E_x and H_y components to solve for the dispersion relation and the modal fields in moving-slab waveguide. Note that for a fair comparison between the stationary and moving waveguide properties, it should be ensured that only E_x field is conserved in the calculations of the moving waveguide, because the fields perpendicular to the direction of propagation are not conserved as per Lorentz transformation. Other field components must be computed as per Eqs. (10) and (11). For computation of optical force, $E_x = 1e^{i(k_x x - \omega t)} e^{ik_{z2} z}$ V/m, is assumed in the region $z > d/2$.

Appendix B. Optical forces on a chiral particle

A chiral particle is characterized by its polarizability matrix $\begin{bmatrix} \alpha_{ee} & i\alpha_{em} \\ -i\alpha_{me} & \alpha_{mm} \end{bmatrix}$, which is defined as $\begin{bmatrix} \vec{p} \\ \vec{m} \end{bmatrix} = \begin{bmatrix} \alpha_{ee} & i\alpha_{em} \\ -i\alpha_{me} & \alpha_{mm} \end{bmatrix} \begin{bmatrix} \vec{E} \\ \vec{H} \end{bmatrix}$. Here $\vec{p}$ is the electric dipole moment and $\vec{m}$ is the magnetic

dipole. The coefficients of polarizability matrix of the chiral particle is assumed to be [6, 15] $\alpha_{ee} = (1.2 + i0.01) \times 10^{-24} Cm^2/V$, $\alpha_{mm} = 0.0002 \times 10^{-24} m^3$, $\alpha_{em} = 0.01 \times 10^{-24} Cm^2/A$ and $\alpha_{me} = 0.01 \times 10^{-24} Am^3/V$.

The optical forces acting on this chiral particle are given by [6, 15],

$$\langle \vec{F} \rangle = \langle \vec{F}_{gr} \rangle + \langle \vec{F}_{op} \rangle + \langle \vec{F}_{sr} \rangle, \tag{17}$$

$$\langle \vec{F}_{gr} \rangle = \nabla U, \tag{18}$$

$$\langle \vec{F}_{op} \rangle = \frac{k_0}{c} \left(\frac{Im[\alpha_{ee}]}{\epsilon_0} + \frac{Im[\alpha_{mm}]}{\mu_0} \right) \langle \vec{N} \rangle - Im[\alpha_{em}] \nabla \times \langle \vec{N} \rangle$$
$$- \frac{ck_0}{2} \left(\frac{Im[\alpha_{ee}]}{\epsilon_0} \nabla \times \langle \vec{s}_e \rangle + \frac{Im[\alpha_{mm}]}{\mu_0} \nabla \times \langle \vec{s}_m \rangle \right) \tag{19}$$
$$+ \omega^2 Im[\alpha_{em}] \left(\langle \vec{s}_e \rangle + \langle \vec{s}_m \rangle \right),$$

$$\langle \vec{F}_{sr} \rangle = -\frac{ck_0^4}{6\pi} \left\{ \left(Re[\alpha_{ee}\alpha_{mm}^*] + |\alpha_{em}|^2 \right) \langle \vec{N} \rangle + \sqrt{\frac{\mu_0}{\epsilon_0}} Re[\alpha_{ee}\alpha_{em}^*] \vec{S}_3^e \right.$$
$$\left. + \sqrt{\frac{\epsilon_0}{\mu_0}} Re[\alpha_{mm}\alpha_{em}^*] \vec{S}_3^m - \frac{1}{2} Im[\alpha_{ee}\alpha_{mm}^*] Im[\vec{E} \times \vec{H}^*] \right\}, \tag{20}$$

where $k_0 = \omega/c$, $\langle \vec{N} \rangle = 1/2 Re\{\vec{E} \times \vec{H}^*\}$, and $U = 1/4(Re[\alpha_{ee}]|\vec{E}|^2 + Re[\alpha_{mm}]|\vec{H}|^2 - 2Re[\alpha_{em}]Im[\vec{H} \cdot \vec{E}^*])$. $\langle \vec{F}_{gr} \rangle$ is gradient force, $\langle \vec{F}_{op} \rangle$ is optical pressure force, and $\langle \vec{F}_{sr} \rangle$ is scattering recoil force. The expressions for the forces are derived from Maxwell stress tensor [43], $\overleftrightarrow{T}$,

$$T_{ij} = \epsilon_0 \left(E_i E_j - \frac{1}{2} \delta_{ij} E^2 \right) + \frac{1}{\mu_0} \left(B_i B_j - \frac{1}{2} \delta_{ij} B^2 \right), \tag{21}$$

$$\vec{F} = \oint_{\partial \nu} \overleftrightarrow{T} \cdot \vec{a}. \tag{22}$$

where $\partial \nu$ is a closed surface enclosing the particle and $\vec{a}$ is normal to that surface.

These optical forces are computed from the fields at a distance of $0.1d$, which corresponds to $0.15\mu m$. The frequency ω of the modes in stationary waveguide is assumed to be $2\pi 10^{14}$rad/s. For the moving waveguide, the frequency is transformed as per the transformation of dispersion curve [Fig. 2(b)].

Funding

References

1. P. Lodahl, S. Mahmoodian, S. Stobbe, A. Rauschenbeutel, P. Schneewiss, J. Volz, H. Pichler, and P. Zoller, "Chiral quantum optics," Nature **541**, 473 (2017).
2. A. S. Urban, S. Carretero-Palacios, A. A. Lutich, T. Lohmüller, J. Feldmann, and F. Jäckel, "Optical trapping and manipulation of plasmonic nanoparticles: fundamentals, applications, and perspectives," Nanoscale **6**, 4458–4474 (2014).

3. T. Zhang, M. R. C. Mahdy, Y. Liu, J. H. Teng, C. T. Lim, Z. Wang, and C.-W. Qiu, "All-optical chirality-sensitive sorting via reversible lateral forces in interference fields," ACS Nano **11**, 4292–4300 (2017).

4. A. Canaguier-Durand, J. A. Hutchison, C. Genet, and T. W. Ebbesen, "Mechanical separation of chiral dipoles by chiral light," New J. Phys. **15**, 123037 (2013).

5. F. Le Kien, S. S. S. Hejazi, V. G. Truong, S. Nic Chormaic, and T. Busch, "Chiral force of guided light on an atom," Phys. Rev. A **97**, 063849 (2018).

6. S. Wang and C. Chan, "Lateral optical force on chiral particles near a surface," Nat. Commun. **5**, 4307 (2014).

7. M. Antognozzi, C. Bermingham, R. Harniman, S. Simpson, J. Senior, R. Hayward, H. Hoerber, M. Dennis, A. Bekshaev, K. Bliokh, and F. Nori, "Direct measurements of the extraordinary optical momentum and transverse spin-dependent force using a nano-cantilever," Nat. Phys. **12**, 731 (2016).

8. L. Liu, A. Di Donato, V. Ginis, S. Kheifets, A. Amirzhan, and F. Capasso, "Three-dimensional measurement of the helicity-dependent forces on a mie particle," Phys. Rev. Lett. **120**, 223901 (2018).

9. S. Scheel, S. Y. Buhmann, C. Clausen, and P. Schneeweiss, "Directional spontaneous emission and lateral casimir-polder force on an atom close to a nanofiber," Phys. Rev. A **92**, 043819 (2015).

10. F. J. Rodríguez-fortuño, N. Engheta, A. Martínez, and A. V. Zayats, "Lateral forces on circularly polarizable particles near a surface," Nat. Commun. **6**, 8799 (2015).

11. M. H. Alizadeh and B. M. Reinhard, "Transverse chiral optical forces by chiral surface plasmon polaritons," ACS Photonics **2**, 1780–1788 (2015).

12. S. Sukhov, V. Kajorndejnukul, R. R. Naraghi, and A. Dogariu, "Dynamic consequences of optical spin–orbit interaction," Nat. Photonics **9**, 809 (2015).

13. M. Neugebauer, T. Bauer, P. Banzer, and G. Leuchs, "Polarization tailored light driven directional optical nanobeacon," Nano Lett. **14**, 2546–2551 (2014).

14. R. P. Cameron, S. M. Barnett, and A. M. Yao, "Discriminatory optical force for chiral molecules," New J. Phys. **16**, 013020 (2014).

15. F. Kalhor, T. Thundat, and Z. Jacob, "Universal spin-momentum locked optical forces," Appl. Phys. Lett. **108**, 061102 (2016).

16. T. Van Mechelen and Z. Jacob, "Universal spin-momentum locking of evanescent waves," Optica **3**, 118–126 (2016).

17. K. Y. Bliokh, D. Smirnova, and F. Nori, "Quantum spin hall effect of light," Science **348**, 1448–1451 (2015).

18. J. Maciejko, T. L. Hughes, and S.-C. Zhang, "The quantum spin hall effect," Annu. Rev. Condens. Matter Phys. **2**, 31–53 (2011).

19. L. Cai, M. Liu, S. Chen, Y. Liu, W. Shu, H. Luo, and S. Wen, "Quantized photonic spin hall effect in graphene," Phys. Rev. A **95**, 013809 (2017).

20. L. Huang, X. Chen, B. Bai, Q. Tan, G. Jin, T. Zentgraf, and S. Zhang, "Helicity dependent directional surface plasmon polariton excitation using a metasurface with interfacial phase discontinuity," Light. Sci. & Appl. **2**, e70 (2013).

21. J. Petersen, J. Volz, and A. Rauschenbeutel, "Chiral nanophotonic waveguide interface based on spin-orbit interaction of light," Science **346**, 67–71 (2014).

22. D. O'Connor, P. Ginzburg, F. Rodríguez-Fortuño, G. Wurtz, and A. Zayats, "Spin-orbit coupling in surface plasmon scattering by nanostructures." Nat. Commun. **5**, 5327 (2014).

23. R. Mitsch, C. Sayrin, B. Albrecht, P. Schneeweiss, and A. Rauschenbeutel, "Quantum state-controlled directional spontaneous emission of photons into a nanophotonic waveguide," Nat. Commun. **5**, 5713 (2014).

24. W. Ye, F. Zeuner, X. Li, B. Reineke, S. He, C.-W. Qiu, J. Liu, Y. Wang, S. Zhang, and T. Zentgraf, "Spin and wavelength multiplexed nonlinear metasurface holography," Nat. Commun. **7**, 11930 (2016).

25. A. Espinosa-Soria and A. Martĩnez, "Transverse spin and spin-orbit coupling in silicon waveguides," IEEE Photonics Technol. Lett. **28**, 1561–1564 (2016).

26. D. F. Kornovan, A. S. Sheremet, and M. I. Petrov, "Collective polaritonic modes in an array of two-level quantum emitters coupled to an optical nanofiber," Phys. Rev. B **94**, 245416 (2016).

27. I. Söllner, S. Mahmoodian, S. L. Hansen, L. Midolo, A. Javadi, G. Kiršanskė, T. Pregnolato, H. El-Ella, E. H. Lee, J. D. Song, S. Stobbe, and P. Lodahl, "Deterministic photon–emitter coupling in chiral photonic circuits," Nat. nanotechnology **10**, 775–778 (2015).

28. B. le Feber, N. Rotenberg, and L. Kuipers, "Nanophotonic control of circular dipole emission," Nat. Commun. **6**, 6695 (2015).

29. J. Lin, J. P. B. Mueller, Q. Wang, G. Yuan, N. Antoniou, X.-C. Yuan, and F. Capasso, "Polarization-controlled tunable directional coupling of surface plasmon polaritons," Science **340**, 331–334 (2013).

30. A. Espinosa-Soria, F. J. Rodrĩguez-Fortuĩo, A. Griol, and A. Martĩnez, "On-chip optimal stokes nanopolarimetry based on spin–orbit interaction of light," Nano Lett. **17**, 3139–3144 (2017). PMID: 28388061.

31. J. B. González-Díaz, A. García-Martín, G. Armelles, J. M. García-Martín, C. Clavero, A. Cebollada, R. Lukaszew, J. Skuza, D. Kumah, and R. Clarke, "Surface-magnetoplasmon nonreciprocity effects in noble-metal/ferromagnetic heterostructures," Phys. Rev. B **76**, 153402 (2007).

32. Y. Shoji and T. Mizumoto, "Magneto-optical non-reciprocal devices in silicon photonics," Sci. Technol. Adv. Mater. **15**, 014602 (2014).

33. F. Ruesink, M.-A. Miri, A. Alù, and E. Verhagen, "Nonreciprocity and magnetic-free isolation based on optomechanical interactions," Nat. Commun. **7**, 13662 (2016).

34. Z. Shen, Y.-L. Zhang, Y. Chen, C.-L. Zou, Y.-F. Xiao, X.-B. Zou, F.-W. Sun, G.-C. Guo, and C.-H. Dong,

"Experimental realization of optomechanically induced non-reciprocity," Nat. Photonics **10**, 657–661 (2016).

35. H. C. Lefevre, *The fiber-optic gyroscope* (Artech house, 2014).

36. N. A. Estep, D. L. Sounas, J. Soric, and A. Alù, "Magnetic-free non-reciprocity and isolation based on parametrically modulated coupled-resonator loops," Nat. Phys. **10**, 923 (2014).

37. R. Luo, Y. Li, S. Deng, D. He, C. Peng, and Z. Li, "Compensation of thermal strain induced polarization nonreciprocity in dual-polarization fiber optic gyroscope," Opt. Express **25**, 26747–26759 (2017).

38. R. Luo, Y. Li, S. Deng, C. Peng, and Z. Li, "Effective suppression of residual coherent phase error in a dual-polarization fiber optic gyroscope," Opt. Lett. **43**, 815–818 (2018).

39. R. R. O. Weernink, P. Barcellona, and S. Y. Buhmann, "Lateral casimir-polder forces by breaking time-reversal symmetry," Phys. Rev. A **97**, 032507 (2018).

40. J. A. Kong, *Theory of electromagnetic waves* (Wiley-Interscience, 1975).

41. S. Pendharker, Y. Guo, F. Khosravi, and Z. Jacob, "PT-symmetric spectral singularity and negative-frequency resonance," Phys. Rev. A **95**, 033817 (2017).

42. T. Van Mechelen and Z. Jacob, "Quantum gyro-electric effect: Photon spin-1 quantization in continuum topological bosonic phases," arXiv preprint arXiv:1806.01395 (2018).

43. D. J. Griffith and G. Ruppeiner, *Introduction to Electrodynamics* (AAPT, 1981).